Real-Time Microscale Temperature Imaging by Stimulated Raman Scattering

Benjamin Figueroa[†], *Rachel Hu*[†], *Samuel G. Rayner*[‡,§], *Ying Zheng*[‡], *Dan Fu*[†,*]

[†]Department of Chemistry, University of Washington, Seattle, Washington, 98195, USA

[‡]Department of Bioengineering, University of Washington, Seattle, Washington, 98195, USA

[§]Department of Medicine, Division of Pulmonary, Critical Care and Sleep Medicine, University of Washington, Seattle, WA, 98109, USA

AUTHOR INFORMATION

Corresponding Author

*Dan Fu – Department of Chemistry, University of Washington, Seattle, Washington, 98195, USA

ABSTRACT: Microscale thermometry of aqueous solutions is essential to understand the dynamics of local heat generation and dissipation in chemical and biological systems. A wide variety of fluorescent probes have been developed to map temperature changes with submicron resolution, but they often suffer from the uncertainty associated with microenvironment dependent fluorescent properties. In this work, we develop a label-free ratiometric stimulated Raman scattering (SRS) microscopy technique to quantify microscale temperature by monitoring the O-

H Raman stretching modes of water. By tracking the ratio changes of the hydrogen-bonding O-H band and the isosbestic band, we can directly quantify the temperature of water-based environments in real-time without exogenous contrast agents. We demonstrate real-time measurement of localized intracellular and extracellular-temperature changes due to laser absorption. This high-speed nonlinear optical imaging technique has the potential for *in situ* microscale imaging of thermogenesis in both chemical and biological systems.

TOC GRAPHIC

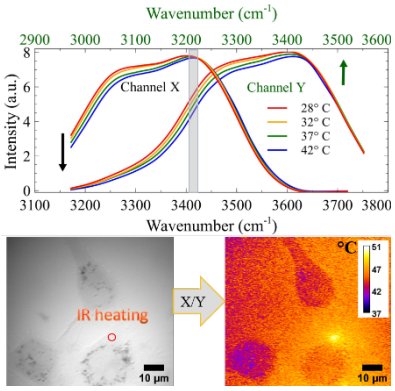

KEYWORDS Label-free microscopy, Thermal imaging, nonlinear microscopy, optical heating, Raman scattering.

Temperature is a fundamental parameter in determining chemical reaction rates as dictated by the Arrhenius equation. Such dependence is also essential in biological systems. In mammals, body temperature is strictly regulated to maintain cell homeostasis through a careful balance of heat generation and heat dissipation.[1,2] Aberrant temperatures can cause cell death through apoptosis and necrosis.[3] This effect has been utilized in photothermal therapy for targeted tumor ablation and in cold therapy for fat loss.[4,5] It is essential to monitor the temperature in biological cells to

understand body physiology and to develop new therapeutic approaches. While temperature can be easily measured with either a contact-type thermal couple or non-contact infrared thermography, the spatial resolution has been typically limited to tens of micrometers or worse.

To image temperature distribution at micrometer resolution for intracellular temperature measurements, a wide variety of fluorescence temperature sensors including temperature-sensitive fluorescent polymers,[6] quantum dots,[7] nanodiamonds,[8] and fluorescent proteins[9] have been developed. Fluorescent thermosensors offer sub-degree temperature sensitivity and provide the dual function of imaging and temperature sensing. To improve robustness of intracellular measurements, ratiometric imaging or fluorescence lifetime imaging is employed, which overcomes the limitations of intensity-based imaging.[6,9]

A wide range of intracellular temperature gradients has been reported with various fluorescent sensors. For example, mitochondria temperature was reported to be anywhere from 1°C to 10°C warmer than the cytoplasm.[9–11] While some of these variations may reflect biological differences, others could also be attributed to measurement bias due to environmental influences on fluorescence.[12] Recent debate on the validity of fluorescence based intracellular temperature measurements further highlight the need for rigorous validation, especially with orthogonal label-free techniques for accurate temperature measurement.[13–15]

Raman spectroscopy has shown promise for temperature measurement with prior reports estimating temperature by measuring the ratio of anti-Stokes to Stokes scattering.[16] However, its sensitivity is limited to ~10°C.[17] In a related technique, Raman spectroscopy can also monitor water temperature based on changes in hydrogen bonding. The OH stretching band of water has two inversely related temperature-dependent modes: the hydrogen-bonded (HB) and non-

hydrogen-bonded (NHB) modes at 3200 and 3600 cm^{-1}, respectively. As the temperature increases, the hydrogen bonding of clustered water molecules is broken, and the number of non-hydrogen-bonded water molecules increases. Temperature is linearly correlated to the ratio of these two modes.[18] This phenomenon has been previously used to determine water temperature with precision reaching 0.1°C, which is comparable to fluorescence thermometry.[18,19] However, as Raman scattering is a weak process, this technique has been limited to point measurements in systems at steady states. It is thus not suitable for temperature imaging of dynamic biological specimens.

Here, we describe the development of a stimulated Raman scattering (SRS) based thermometry technique utilizing fast ratiometric imaging of two water Raman bands for microscale temperature mapping. SRS improves the Raman scattering efficiency by more than 6 orders of magnitude through coherent excitation. Indeed, SRS microscopy has been widely used in favor of spontaneous Raman microscopy for cellular and tissue imaging due to its superior imaging speed.[20,21] Using our previously developed broadband fiber laser[22] and a dual-channel orthogonal modulation scheme, we perform real-time ratiometric SRS imaging of the HB and NHB modes of water and map microscale temperature distribution. We demonstrate quantification of heat generation from a laser point source in aqueous and biological samples and the capability to extract the thermal conductivities of subcellular components. This advancement paves the way for real-time label-free *in vivo* imaging of microscale intracellular thermogenesis.

To image two Raman bands simultaneously for ratiometry, we use a two-channel orthogonal modulation technique that was recently developed for SRS imaging with spectral focusing (Figure S1).[23,24] Details of the experimental setup and detection scheme are provided in the Supplementary Information. Briefly, two orthogonally modulated Stokes pulses train are combined with the pump

beam for excitation of two different Raman bands that are determined by their respective pump-Stokes time delay. The lock-in amplifier outputs in the X channel and Y channel provide two independent readings of SRS signals at these two Raman bands. The original orthogonal modulation method is highly sensitive to the optical alignment due to the requirement for precise spatial and temporal overlap of three different beams. We address this shortcoming by using two electro-optical modulators to perform orthogonal modulation, thus obviating the need for alignment of two separate Stokes beams (Figure S1). Due to the limited bandwidth of the SRS pump and Stokes lasers (150 cm^{-1} and 60 cm^{-1}, respectively), existing SRS systems based on spectral focusing cannot reliably probe both temperature-dependent Raman bands. We use our previously developed parabolic fiber amplifier to increase spectral bandwidth of the Stokes laser to ~ 500 cm^{-1} (Figure S2).[22] We calibrated Raman frequency using SRS imaging of urea crystals

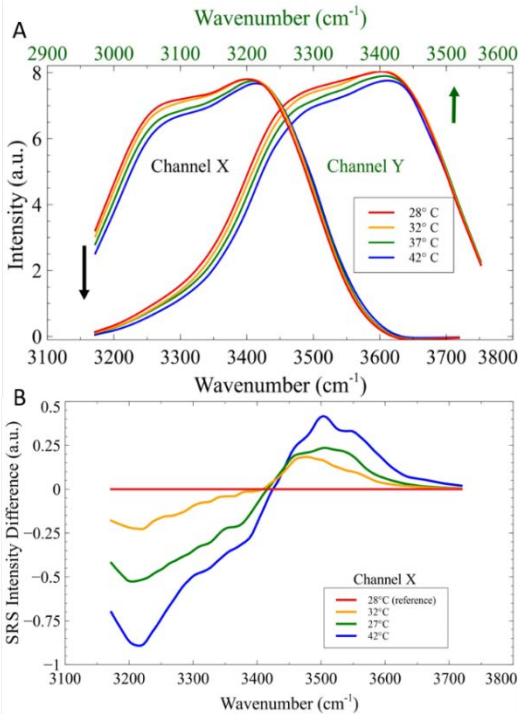

Figure 1. A) Simultaneous collection of 2-channel SRS spectra arising from OH stretching vibrations of liquid H2O at different temperatures. B) SRS difference spectra calculated from the spectra of channel X.

(Figure S3). The broadband laser source allows for the simultaneous acquisition of the two temperature-dependent Raman bands.

To determine the temperature-induced spectral changes on water, SRS spectra at different temperatures were recorded by scanning the time delay between the pump and the two orthogonally modulated Stokes beams. The pump beam was tuned to 779 nm to optimize detection of the OH vibrational band with the 1050 nm Stokes beams. Figure 1A shows water SRS spectra collected from the two orthogonal SRS channels (i.e. Channel X and Channel Y from the lock-in amplifier) from 3050-3700 cm^{-1}. As shown in Figure 1A, the SRS intensity below the isosbestic point (~3450 cm^{-1}) decreases with a temperature rise, while the intensity above the isosbestic point slightly increases. This is due to changes in equilibrium between the HB and the NHB water molecules. The isosbestic point is observed near 3450 cm^{-1}, comparable to previously reported values.[18,25] To show the spectral change more clearly, Raman difference spectra were calculated from Figure 1A by subtracting the reference spectrum at 28°C from other spectra (Figure 1B). It is evident that the OH stretching band of water has two modes with contrasting temperature dependencies: a negative peak at ~3220 cm^{-1} and a positive peak around 3550 cm^{-1}. Previous Raman thermometry studies monitored the ratio of 3200/3600 cm^{-1} to maximize temperature sensitivity. Our difference spectra peaks deviate slightly from previous reports. This deviation can be attributed to the limited spectral bandwidth of SRS which reshapes the NHB band towards lower wavenumbers and lower spectral resolution of our SRS microscope (~30 cm^{-1}). For our study, we focus on the ratio between the HB and isosbestic band because the isosbestic SRS band intensity near 3420 cm^{-1} is much higher than at 3550 cm^{-1}, which offers higher SNR in imaging.

To correlate temperature with SRS intensity ratio of $I_{3220cm\text{-}1}/I_{3420\ cm\text{-}1}$ (I_{ratio}), calibration experiments were performed under uniform temperature conditions using a temperature-controlled

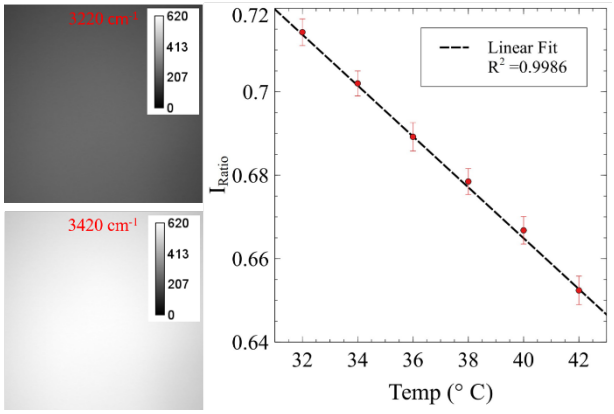

Figure 2. Left) SRS intensity images of the hydrogen bonded channel and isosbestic channel at 3220 and 3420 cm^{-1}, respectively. Right) Temperature calibration showing the linear relationship between temperature and SRS intensity ratio (I_{Ratio}).

chamber. Absolute temperature of water was determined by a miniature thermistor placed inside the chamber. For each temperature, 10 SRS image pairs were acquired at 1 frame/sec. These images were averaged and the I_{ratio} image was determined by dividing the HB channel (~3220 cm^{-1}) by the isosbestic channel (~3420 cm^{-1}). We would like to note that although we use frame averaging to increase the sensitivity, within each frame the temperature at each pixel (4 µs pixel dwell time) reflects instantaneous temperature. The averaging of 10 frames reduces noise and may average out temperature changes between frames if there is accumulated heating. Figure 2 shows the relationship between temperature and I_{ratio}. As expected, I_{ratio} scales linearly with temperature. The standard deviation of the intensity ratio for each averaged I_{ratio} image is indicated as the error bar. Error estimates were performed at the center of the image as SRS intensity is highest at the center. This effect is caused by the chromatic aberration of the objective lens. Based on the calibration curve and measured intensity ratio error, we determine that SRS thermometry provides a temperature imaging accuracy of 0.53°C (close to the edge of the image, the error increases to 0.69°C), which is comparable to many fluorescent temperature sensors.[6,10,26–28]

Next, we apply SRS thermometry to directly quantify laser induced heating in water. Photothermally induced heating has been used increasingly as a tool for microscopic manipulation in biology, such as photothermal therapy.[29] While various studies have focused on simulating heating by absorption in the focus of an objective for the optimization of laser parameters (e.g. wavelength, irradiation intensity, penetration depth, spot size, etc),[30,31] experimental studies of microscale temperature change due to laser heating have been mostly limited to optical tweezer experiments.[32] To visualize the temperature gradient induced by a focused infrared laser beam, we coupled a continuous wave 1480 nm fiber laser diode via the side port of the inverted microscope (bypassing the galvo scan mirrors) to provide localized heating in our imaging field of view. The

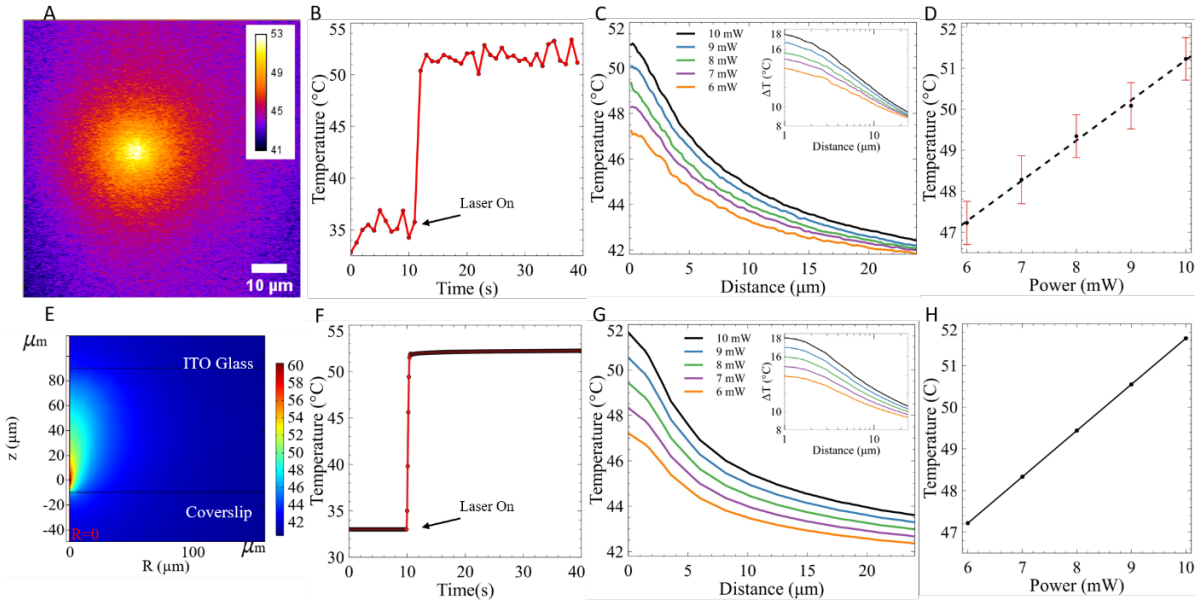

Figure 3. Experimental and simulated temperature distribution generated by a focused IR laser. A) Temperature mapping of laser induced heating by a 1480 nm IR laser source in water. B) Temporal profile of temperature at the center of the laser spot C) Radial profiles of temperature gradient at different IR irradiation powers (log scale plot in inset) D) Peak temperature of the localized heating source as a function of irradiation power. E) Simulation of heating source near the coverslip boundary. F-H) Simulated counterparts of B-D).

heating laser was focused onto the sample, producing a temperature gradient around the heating spot. The SRS image of the temperature distribution is shown in Figure 3A by converting I_{ratio} into temperature using the calibration demonstrated in Figure 2. We observed a maximum temperature rise of ~16°C induced by 10 mW irradiation power. Time-lapse imaging shows that temperature rise happens in less than a second, below the temporal resolution of our system (Figure 3B). This sub-second rapid heating reaches an equilibrium of ~ 51°C at the focal point and decreases rapidly away from the focus. Figure 3C plots the radial temperature profile as a function of irradiation intensity. Maximal temperature increase at the laser focus depends linearly on the optical power (Figure 3D).

To verify these results, we used the finite element method provided within COMSOL modeling software to solve the heat transport equation with appropriate initial and boundary conditions (see Supporting Information). In contrast to previous reports where laser induced heating was modeled in a region distant from the boundaries,[33,34] the temperature gradient arising from a stationary laser spot 10 μm above the coverslip was modeled, resulting in an axially asymmetrical temperature gradient arising from the coverslip boundary (Figure 3E). Analysis of the simulated radial thermal decay from the center of the laser spot reveals similar peak temperature profiles compared to our experimental conditions. We note that the temperature profile depends on how far the imaging plane deviates from the heating spot (Figure S4). In our simulation (Figure 3G), a separation of 7 μm provides best matching of simulation to experimental results, suggesting that the axial chromatic aberration of IR heating laser and SRS lasers may give rise to lower observed temperature gradients. Other factors may also influence experimental measurements, including the size of the IR laser focus and the distance of the laser focus to the coverslip. Nevertheless, both our experiment and simulation results show that at 2-3 μm away from the heating focus, the

temperature follows a logarithmic decay with the distance r away from the laser focus via the model proposed by Mao *et al*., $\Delta T = \frac{\alpha(\lambda)*P}{2\pi k} * ln(r)$ (Figure 3C,G insets).[33,34] Here α is the frequency dependent absorption coefficient of water (2100 m^{-1}), P is laser power (10mW), and k is thermal conductivity of the medium. As seen in Figures 3B and S2B, the slope of the model will be affected by the proximity of the heating source to the coverslip and therefore the equation needs to be modified with an additional correction factor that is a function of geometrical arrangement and laser focus property. Importantly, the agreement between simulations and experiments suggest that the heat diffusion equation holds at the micrometer scale, which is important for modeling heat diffusion inside the cell.[14]

We note that while measuring temperature increase due to an external laser source is valuable with respect to photothermal therapy, the heating due to the imaging lasers is also important to consider for many imaging applications. Indeed, photodamage in nonlinear optical microscopy is a common concern in the field due to the high optical powers often used in live cell or animal imaging.[35] Direct measurement of temperature change due to nonlinear optical microscopy is scarce.[36,37] Using SRS thermometry, we demonstrate the ability to directly measure the temperature increase due to SRS imaging (Figure 3F). Specifically, the first few seconds (before the external laser is applied) see an increase of ~2°C. This temperature increase is due to the combined effect of linear absorption of the pump and Stokes beams as well as heat dissipation from the SRS process. Based on thermistor measurements, absorption of SRS excitation beams is the dominant source of heating. This temperature increase due to imaging is often insufficient to cause thermal damage but may cause physiological changes.[37,38] Therefore, SRS imaging

experiments on living biological samples should limit total power to ~100 mW to avoid potential damage and incorrect interpretation of cell physiology, especially for longitudinal imaging.

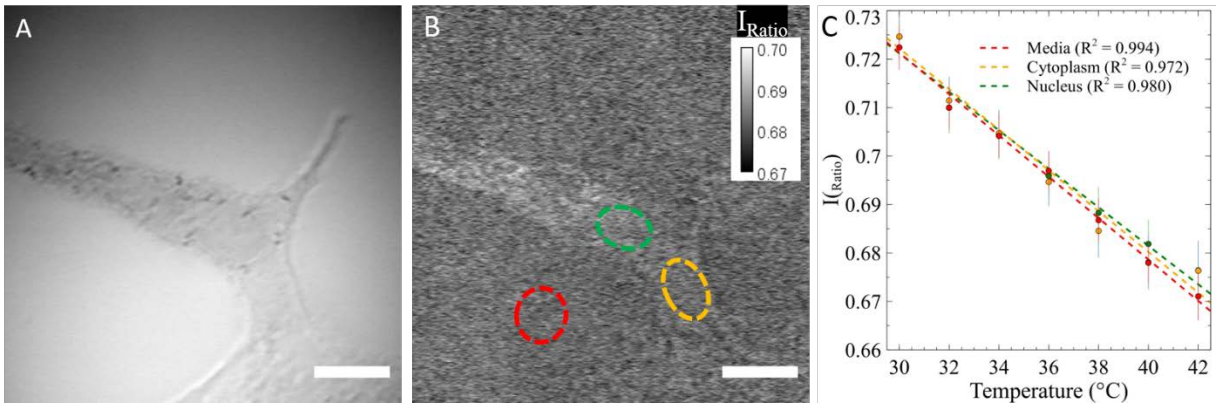

Figure 4. SRS Thermometry on fixed A549 cells kept at 37°C. Representative A) SRS image at 3420 cm^{-1} and B) SRS thermal map. C) Temperature calibration of intra and extracellular components. The scale bar 10 is μm.

Next, we measure the thermal conductivity of cellular materials using our SRS-based thermometry technique. Thermal conductivity is a key parameter in determining the temperature rise in the presence of a heat source. Within the cell, the mitochondrion is considered the "power house" and its energy production may create a heat gradient within the cell. Previous reports on the mitochondria temperature vary widely from 1°C to 10°C above the cytoplasm. However, theoretical arguments based on thermal generation and heat diffusion suggest that temperature rise of mitochondria should be a few orders of magnitude smaller.[13] One crucial element in this debate is the thermal conductivity in the presence of a membrane. Here we use SRS thermometry to show that membrane structure does not change the thermal conductivity significantly.

We first created calibration curves by varying the extracellular temperature of fixed A549 cells using the temperature-controlled chamber and imaged with ratiometric SRS. It is important to note

that cellular materials have other components (lipids, protein, and salts etc.) that may influence the water SRS spectrum (Figure S5). Therefore, the calibration of cell temperature needs to account for these components. Figure 4A displays a representative SRS image at 3420 cm^{-1} of a fixed cell with its I_{ratio} image at 37°C shown in Figure 4B. Because there is no heat source, we assume that the temperature throughout the cell is uniform. Figure 4C shows the relationship between temperature and I_{ratio} for different cellular compartments at temperatures between 30-42°C.

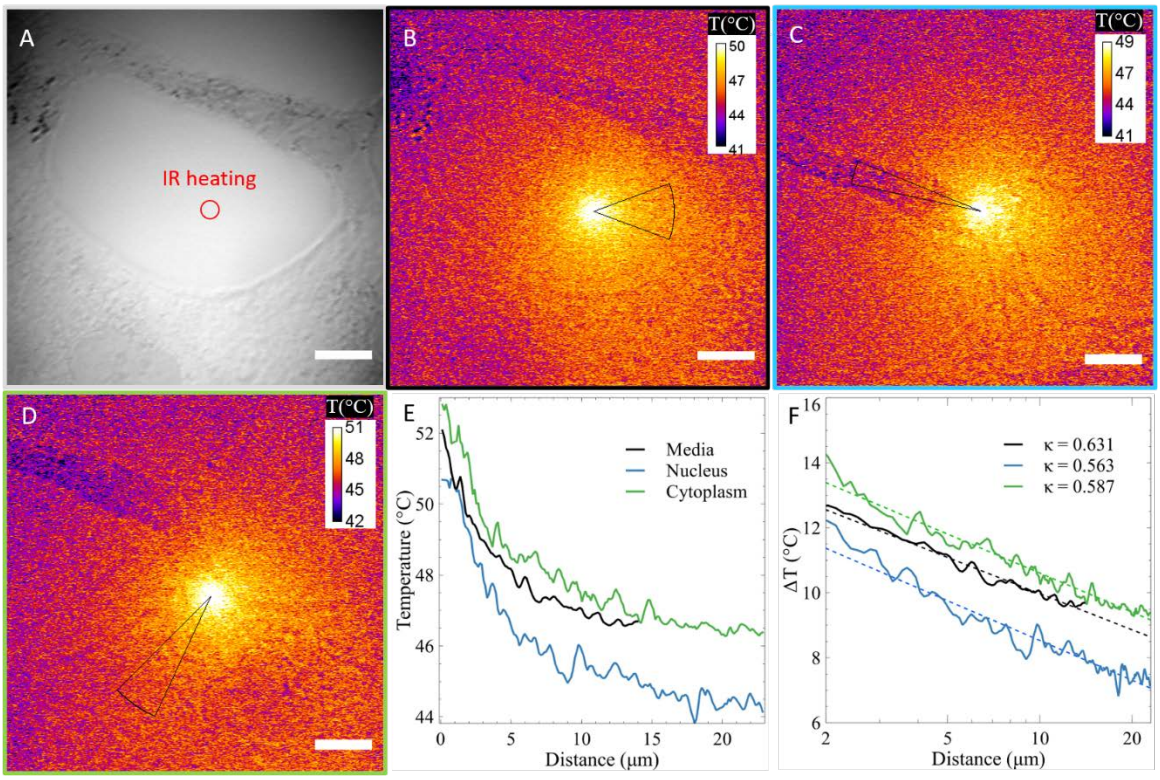

Figure 5. IR heating on extracellular and intracellular material of a fixed A549 cell. A) 3420 cm^{-1} Raman transition showing the heating location on the media with boxes indicating representative regions of interest. SRS temperature image (average of 10 frames) of IR heating on the B) media, C) nucleus, and D) cytoplasm with their respective ROIs for radial profiling. E) Thermal decay curves from each ROI. D) Log scale plots with slopes converted to thermal conductivities for each component. The scale bar is 10 μm.

Although there are slight spectral differences between the cellular components, we observe that the calibration slope difference between intracellular and extracellular material is relatively small at <0.0017, suggesting that cellular materials and their compositional variation have little influence on the calibration curve. Due to the nonuniformity of the sample, the accuracy of temperature calibration is lower compared to bulk water. From the standard deviation of the I_{Ratio}, we estimated that accuracy to be ~ 1.2°C .

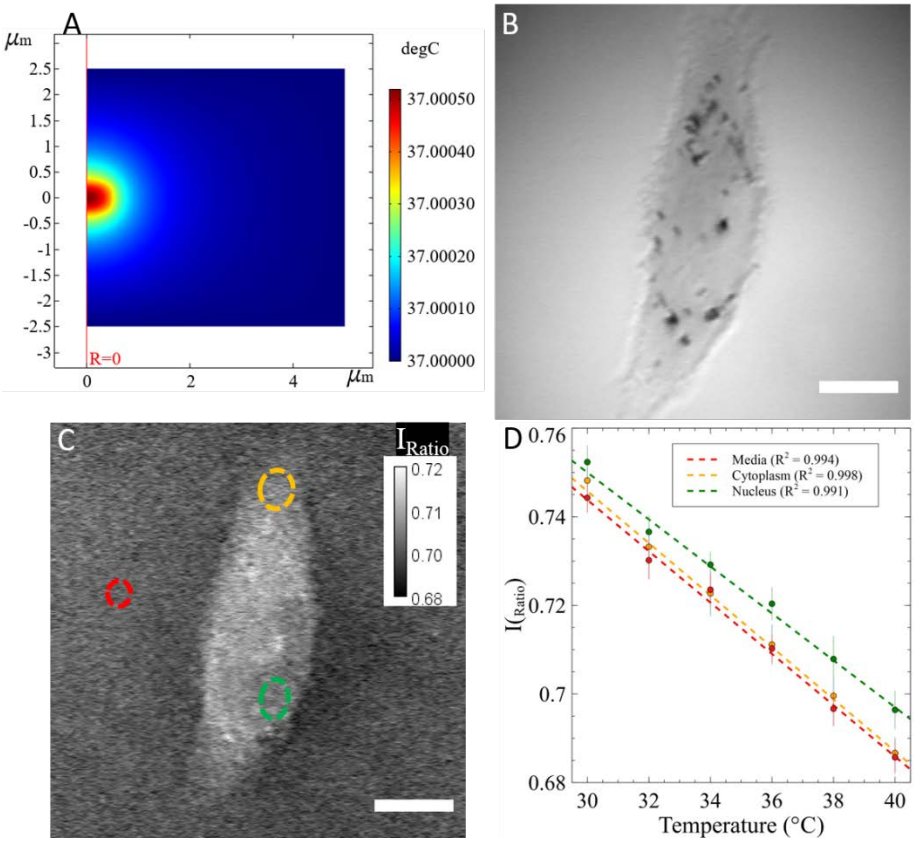

Figure 6. A) Simulation of a single mitochondrial heating within a cell set at 37°C. B-D) SRS Thermometry on live A549 cells kept at 37°C. Representative B) SRS image at 3420 cm^{-1} and C) SRS thermal map. D) Temperature calibration of intra and extracellular components. The scale bar is 10 μm.

Next, we performed laser heating inside the fixed cell to extract thermal conductivity values via the amended model of Mao *et al.*[33] The temperature gradient can be estimated by $\Delta T = C\frac{\alpha(\lambda)*P}{2\pi k} *$

$ln(r)$, where C is the correction factor that accounts for distance to the heat sink, aberration, and other geometric factors. For a given geometry, ΔT is inversely proportional to the thermal conductivity k. We can obtain a proportionality constant from the slope which will enable the extraction of k within cells based on the known value of water. By moving the sample relative to the IR laser focus, we determined the logarithmic slope of the radial temperature decay profile for cytoplasm, nucleus, and extracellular region. Only the range of distance r where it satisfies the logarithmic linear model and does not cross any cellular boundaries were used for fitting (cones in Fig 5). Using the known value of k for water (k_{water} ~ 0.631 $W \cdot m^{-1} \cdot K^{-1}$.),[39] we calculated the k values of subcellular regions and found that both the nucleus ($k_{nucleus}$ ~ 0.563 $W \cdot m^{-1} \cdot K^{-1}$) and the cytoplasm ($k_{cytoplasm}$ ~ 0.587 $W \cdot m^{-1} \cdot K^{-1}$) exhibit lower thermal conductivity than water. This agrees with previously reported values showing lower thermal conductivities for intracellular components compared to aqueous solutions.[40] However, the difference is relatively small and would not influence the temperature significantly in the presence of intracellular thermogenesis.

Lastly, we investigated intracellular thermogenesis of mitochondria using COMSOL simulation based on the thermal conductivity measured. We simulated heating distribution from a single mitochondrion within a living cell set at 37°C (Figure 6A). Even when assuming that the average heat generation of the cell (~100 pW/cell)[41,42] originates from a single mitochondrial (L = 500 nm), a temperature change of only $\Delta T \sim 0.0005$°C is expected. This miniscule change is far below the sensitivity limits of current thermography techniques. It also confirms previous theoretical argument by Baffou *et.al.* that intracellular temperature gradient due to mitochondria heating is orders of magnitude than 1°C.[13] When applying our ratiometric SRS imaging to live cells, we observed that unlike fixed cells, live cells exhibit higher ratio than the extracellular media (Figure 6B-D). This does not reflect that live cells have lower temperature, but suggests that other factors

in live cells contribute to the Raman ratio changes, such as the absorption of other molecules or changes in hydrogen bonding dynamics in intracellular compartments.[43,44] Nevertheless, in the temperature calibration experiment, the slopes of Raman ratio with respect to equilibrium temperature stay roughly the same for intracellular space and extracellular media. From the variation of Raman ratios within the cytoplasmic region, we argue that the temperature variation should be less than 0.79°C, which is much less than previous measurements with fluorescent sensors.

In conclusion, we describe the first example of a ratiometric SRS imaging technique for microscale, label-free temperature mapping and quantification. The measurement principle is based on the unique temperature dependence of the Raman band arising from O-H stretching vibrations of H_2O molecules. Using our recently developed broadband laser and an orthogonal modulation technique, two SRS images at 3220 cm^{-1} and 3420 cm^{-1} were simultaneously captured and the intensity ratio of these modes was calculated to determine temperature. Our calibration curve shows a reproducible linear relationship between the temperature and the intensity ratio in the range 30-42°C with a temperature resolution of 0.53°C in pure water.

We demonstrate real-time, label-free monitoring of the intracellular and extracellular-temperature changes of fixed cells under IR heating. Thermal conductivities are extracted by analyzing the thermal decay profiles of external heating on cellular components. Our measurement and simulation on live cells suggest that localized heating by mitochondria would be below 1°C, which cast doubt on the validity of previous endogenous thermogenesis studies reporting rises of a few Kelvins. Further investigation into composition-related spectral change in water-based media will considerably increase the versatility of this technique, which could be applied in future applications such as microfluidic systems for the analysis and control of chemical reactions or

biological processes. Because SRS is a three-dimensional imaging technique, it is also possible to extend this method to *in vivo* applications.

ASSOCIATED CONTENT

Supporting Information.

Experimental and simulation details, wavenumber calibration, thermal profiles as a function of axial position, simulation of mitochondrial heating (PDF)

AUTHOR INFORMATION

ORCID

Benjamin Figueroa 0000-0003-4604-9881

Dan Fu 0000-0001-9243-8306

Notes

Any opinions, finding, and conclusions or recommendations expressed in this material are those of the author(s) and do not necessarily reflect the views of the National Science Foundation. The authors declare no competing financial interest.

ACKNOWLEDGMENT

The work was funded in parts by the NSF CAREER 1846503 to D.F. and NSF GRF DGE-12560682 to B.F.

REFERENCES

(1) Lowell, B. B.; Spiegelman, B. M. Towards a Molecular Understanding of Adaptive Thermogenesis. *Nature* **2000**, *404* (6778), 652–660. https://doi.org/10.1038/35007527.

(2) Blaxter, K. *Energy Metabolism in Animals and Man*; CUP Archive, 1989.

(3) Monti, M.; Brandt, L.; Ikomi-Kumm, J.; Olsson, H. Microcalorimetric Investigation of Cell Metabolism in Tumour Cells from Patients with Non-Hodgkin Lymphoma (NHL). *Scandinavian Journal of Haematology* **1986**, *36* (4), 353–357. https://doi.org/10.1111/j.1600-0609.1986.tb01749.x.

(4) McCabe, K. M.; Hernandez, M. Molecular Thermometry. *Pediatric Research* **2010**, *67* (5), 469–475. https://doi.org/10.1203/PDR.0b013e3181d68cef.

(5) Kim, M.; Lee, J.-H.; Nam, J.-M. Plasmonic Photothermal Nanoparticles for Biomedical Applications. *Advanced Science* **2019**, *6* (17), 1900471. https://doi.org/10.1002/advs.201900471.

(6) Okabe, K.; Inada, N.; Gota, C.; Harada, Y.; Funatsu, T.; Uchiyama, S. Intracellular Temperature Mapping with a Fluorescent Polymeric Thermometer and Fluorescence Lifetime Imaging Microscopy. *Nature Communications* **2012**, *3* (1), 1–9. https://doi.org/10.1038/ncomms1714.

(7) Yang, J.-M.; Yang, H.; Lin, L. Quantum Dot Nano Thermometers Reveal Heterogeneous Local Thermogenesis in Living Cells. *ACS Nano* **2011**, *5* (6), 5067–5071. https://doi.org/10.1021/nn201142f.

(8) Kucsko, G.; Maurer, P. C.; Yao, N. Y.; Kubo, M.; Noh, H. J.; Lo, P. K.; Park, H.; Lukin, M. D. Nanometre-Scale Thermometry in a Living Cell. *Nature* **2013**, *500* (7460), 54–58. https://doi.org/10.1038/nature12373.

(9) Kiyonaka, S.; Kajimoto, T.; Sakaguchi, R.; Shinmi, D.; Omatsu-Kanbe, M.; Matsuura, H.; Imamura, H.; Yoshizaki, T.; Hamachi, I.; Morii, T.; Mori, Y. Genetically Encoded Fluorescent

Thermosensors Visualize Subcellular Thermoregulation in Living Cells. *Nat. Methods* **2013**, *10* (12), 1232–1238. https://doi.org/10.1038/nmeth.2690.

(10) Homma, M.; Takei, Y.; Murata, A.; Inoue, T.; Takeoka, S. A Ratiometric Fluorescent Molecular Probe for Visualization of Mitochondrial Temperature in Living Cells. *Chem. Commun.* **2015**, *51* (28), 6194–6197. https://doi.org/10.1039/C4CC10349A.

(11) Chrétien, D.; Bénit, P.; Ha, H.-H.; Keipert, S.; El-Khoury, R.; Chang, Y.-T.; Jastroch, M.; Jacobs, H. T.; Rustin, P.; Rak, M. Mitochondria Are Physiologically Maintained at Close to 50 °C. *PLOS Biology* **2018**, *16* (1), e2003992. https://doi.org/10.1371/journal.pbio.2003992.

(12) Berezin, M. Y.; Achilefu, S. Fluorescence Lifetime Measurements and Biological Imaging. *Chem. Rev.* **2010**, *110* (5), 2641–2684. https://doi.org/10.1021/cr900343z.

(13) Baffou, G.; Rigneault, H.; Marguet, D.; Jullien, L. A Critique of Methods for Temperature Imaging in Single Cells. *Nature Methods* **2014**, *11* (9), 899–901. https://doi.org/10.1038/nmeth.3073.

(14) Suzuki, M.; Zeeb, V.; Arai, S.; Oyama, K.; Ishiwata, S. The 10 5 Gap Issue between Calculation and Measurement in Single-Cell Thermometry. *Nature Methods* **2015**, *12* (9), 802–803. https://doi.org/10.1038/nmeth.3551.

(15) Baffou, G.; Rigneault, H.; Marguet, D.; Jullien, L. Reply to: "Validating Subcellular Thermal Changes Revealed by Fluorescent Thermosensors" and "The 10 5 Gap Issue between Calculation and Measurement in Single-Cell Thermometry." *Nature Methods* **2015**, *12* (9), 803–803. https://doi.org/10.1038/nmeth.3552.

(16) Meier, B. J. K., Robert J. Determination of the Local Temperature at a Sample during Raman Experiments Using Stokes and Anti-Stokes Raman Bands - Bert J. Kip, Robert J. Meier, 1990. *Applied Spectroscopy* **2016**.

(17) LaPlant, F.; Laurence, G.; Ben-Amotz, D. Theoretical and Experimental Uncertainty in Temperature Measurement of Materials by Raman Spectroscopy. *Appl. Spectrosc., AS* **1996**, *50* (8), 1034–1038.

(18) Kuriyama, R.; Sato, Y. Two-Wavelength Raman Imaging for Non-Intrusive Monitoring of Transient Temperature in Microfluidic Devices. *Meas. Sci. Technol.* **2014**, *25* (9), 095203. https://doi.org/10.1088/0957-0233/25/9/095203.

(19) Liu, K.-L. K.; Davis, K. L.; Morris, M. D. Raman Spectroscopic Measurement of Spatial and Temporal Temperature Gradients in Operating Electrophoresis Capillaries. *Anal. Chem.* **1994**, *66* (21), 3744–3750. https://doi.org/10.1021/ac00093a033.

(20) Cheng, J.-X.; Xie, X. S. Vibrational Spectroscopic Imaging of Living Systems: An Emerging Platform for Biology and Medicine. *Science* **2015**, *350* (6264), aaa8870. https://doi.org/10.1126/science.aaa8870.

(21) Hill, A. H.; Fu, D. Cellular Imaging Using Stimulated Raman Scattering Microscopy. *Analytical Chemistry* **2019**. https://doi.org/10.1021/acs.analchem.9b02095.

(22) Figueroa, B.; Fu, W.; Nguyen, T.; Shin, K.; Manifold, B.; Wise, F.; Fu, D. Broadband Hyperspectral Stimulated Raman Scattering Microscopy with a Parabolic Fiber Amplifier Source. *Biomed. Opt. Express, BOE* **2018**, *9* (12), 6116–6131. https://doi.org/10.1364/BOE.9.006116.

(23) He, R.; Xu, Y.; Zhang, L.; Ma, S.; Wang, X.; Ye, D.; Ji, M. Dual-Phase Stimulated Raman Scattering Microscopy for Real-Time Two-Color Imaging. *Optica* **2017**, *4* (1), 44. https://doi.org/10.1364/OPTICA.4.000044.

(24) Francis, A.; Berry, K.; Chen, Y.; Figueroa, B.; Fu, D. Label-Free Pathology by Spectrally Sliced Femtosecond Stimulated Raman Scattering (SRS) Microscopy. *PLOS ONE* **2017**, *12* (5), e0178750. https://doi.org/10.1371/journal.pone.0178750.

(25) Walrafen, G. E.; Hokmabadi, M. S.; Yang, W. -H. Raman Isosbestic Points from Liquid Water. *J. Chem. Phys.* **1986**, *85* (12), 6964–6969. https://doi.org/10.1063/1.451383.

(26) Gota, C.; Okabe, K.; Funatsu, T.; Harada, Y.; Uchiyama, S. Hydrophilic Fluorescent Nanogel Thermometer for Intracellular Thermometry. *J. Am. Chem. Soc.* **2009**, *131* (8), 2766–2767. https://doi.org/10.1021/ja807714j.

(27) Donner, J. S.; Thompson, S. A.; Kreuzer, M. P.; Baffou, G.; Quidant, R. Mapping Intracellular Temperature Using Green Fluorescent Protein. *Nano Lett.* **2012**, *12* (4), 2107–2111. https://doi.org/10.1021/nl300389y.

(28) Takei, Y.; Arai, S.; Murata, A.; Takabayashi, M.; Oyama, K.; Ishiwata, S.; Takeoka, S.; Suzuki, M. A Nanoparticle-Based Ratiometric and Self-Calibrated Fluorescent Thermometer for Single Living Cells. *ACS Nano* **2014**, *8* (1), 198–206. https://doi.org/10.1021/nn405456e.

(29) Hu, J.-J.; Cheng, Y.-J.; Zhang, X.-Z. Recent Advances in Nanomaterials for Enhanced Photothermal Therapy of Tumors. *Nanoscale* **2018**, *10* (48), 22657–22672. https://doi.org/10.1039/C8NR07627H.

(30) Peterman, E. J. G.; Gittes, F.; Schmidt, C. F. Laser-Induced Heating in Optical Traps. *Biophysical Journal* **2003**, *84* (2), 1308–1316. https://doi.org/10.1016/S0006-3495(03)74946-7.

(31) Schönle, A.; Hell, S. W. Heating by Absorption in the Focus of an Objective Lens. *Opt. Lett., OL* **1998**, *23* (5), 325–327. https://doi.org/10.1364/OL.23.000325.

(32) Català, F.; Marsà, F.; Montes-Usategui, M.; Farré, A.; Martín-Badosa, E. Influence of Experimental Parameters on the Laser Heating of an Optical Trap. *Scientific Reports* **2017**, *7* (1), 1–9. https://doi.org/10.1038/s41598-017-15904-6.

(33) Mao, H.; Ricardo Arias-Gonzalez, J.; Smith, S. B.; Tinoco, I.; Bustamante, C. Temperature Control Methods in a Laser Tweezers System. *Biophysical Journal* **2005**, *89* (2), 1308–1316. https://doi.org/10.1529/biophysj.104.054536.

(34) Haro-González, P.; Ramsay, W. T.; Maestro, L. M.; Rosal, B. del; Santacruz-Gomez, K.; Cruz, M. del C. I. la; Sanz-Rodríguez, F.; Chooi, J. Y.; Sevilla, P. R.; Bettinelli, M.; Choudhury, D.; Kar, A. K.; Solé, J. G.; Jaque, D.; Paterson, L. Quantum Dot-Based Thermal Spectroscopy and Imaging of Optically Trapped Microspheres and Single Cells. *Small* **2013**, *9* (12), 2162–2170. https://doi.org/10.1002/smll.201201740.

(35) Nourhashemi, M.; Mahmoudzadeh, M.; Wallois, F. Thermal Impact of Near-Infrared Laser in Advanced Noninvasive Optical Brain Imaging. *Neurophotonics* **2016**, *3* (1). https://doi.org/10.1117/1.NPh.3.1.015001.

(36) Picot, A.; Dominguez, S.; Liu, C.; Chen, I.-W.; Tanese, D.; Ronzitti, E.; Berto, P.; Papagiakoumou, E.; Oron, D.; Tessier, G.; Forget, B. C.; Emiliani, V. Temperature Rise under

Two-Photon Optogenetic Brain Stimulation. *Cell Rep* **2018**, *24* (5), 1243-1253.e5. https://doi.org/10.1016/j.celrep.2018.06.119.

(37) Podgorski, K.; Ranganathan, G. Brain Heating Induced by Near-Infrared Lasers during Multiphoton Microscopy. *J Neurophysiol* **2016**, *116* (3), 1012–1023. https://doi.org/10.1152/jn.00275.2016.

(38) Doukas, A. G.; Flotte, T. J. Physical Characteristics and Biological Effects of Laser-Induced Stress Waves. *Ultrasound in Medicine & Biology* **1996**, *22* (2), 151–164. https://doi.org/10.1016/0301-5629(95)02026-8.

(39) Appendix B Thermophysical Properties of Water. In *Drying Phenomena*; John Wiley & Sons, Ltd, 2015; pp 457–459. https://doi.org/10.1002/9781118534892.app2.

(40) Kyoo Park, B.; Yi, N.; Park, J.; Choi, T. Y.; Young Lee, J.; Busnaina, A.; Kim, D. Thermal Conductivity of Bovine Serum Albumin: A Tool to Probe Denaturation of Protein. *Appl. Phys. Lett.* **2011**, *99* (16), 163702. https://doi.org/10.1063/1.3652704.

(41) Loesberg, C.; van Miltenburg, J. C.; van Wuk, R. Heat Production of Mammalian Cells at Different Cell-Cycle Phases. *Journal of Thermal Biology* **1982**, *7* (4), 209–213. https://doi.org/10.1016/0306-4565(82)90026-2.

(42) Johnson, M. D.; Völker, J.; Moeller, H. V.; Laws, E.; Breslauer, K. J.; Falkowski, P. G. Universal Constant for Heat Production in Protists. *PNAS* **2009**, *106* (16), 6696–6699. https://doi.org/10.1073/pnas.0902005106.

(43) Nuriya, M.; Yoneyama, H.; Takahashi, K.; Leproux, P.; Couderc, V.; Yasui, M.; Kano, H. Characterization of Intra/Extracellular Water States Probed by Ultrabroadband Multiplex

Coherent Anti-Stokes Raman Scattering (CARS) Spectroscopic Imaging. *J. Phys. Chem. A* **2019**, *123* (17), 3928–3934. https://doi.org/10.1021/acs.jpca.9b03018.

(44) Sugimura, T.; Kajimoto, S.; Nakabayashi, T. Label-Free Imaging of Intracellular Temperature by Using the O−H Stretching Raman Band of Water. *Angewandte Chemie International Edition* **2020**, *59* (20), 7755–7760. https://doi.org/10.1002/anie.201915846.